



An active and robust Si-Fe/N/C catalyst derived from waste reed for oxygen reduction



Qiliang Wei^{a,1}, Xiaohua Yang^{a,1}, Gaixia Zhang^{a,*}, Dongniu Wang^b, Lucia Zuin^b, Dustin Banham^c, Lijun Yang^c, Siyu Ye^c, Youling Wang^a, Mohamed Mohamedi^a, Shuhui Sun^{a,*}

^a Institut National de la Recherche Scientifique-Énergie Matériaux et Télécommunications, Varennes, QC J3X1S2, Canada

^b Canadian Light Source Inc., 44 Innovation Boulevard, Saskatoon, SK S7N 2V3, Canada

^c Ballard Power Systems Inc., Burnaby V5J 5J8, Canada

ARTICLE INFO

Keywords:
Si-Fe/N/C
Graphitization
Pyridinic- and pyrrolic-N
Stable
Oxygen reduction

ABSTRACT

The conversion of biomass waste into valuable carbon composites as efficient non-precious metal oxygen-reduction electrocatalysts is attractive for the development of commercially viable fuel-cell and metal-air battery technologies. Herein, a highly active and robust Si-contained Fe/N/C catalyst is prepared based on the porous carbon deriving from waste reed stalk after carbonization and KOH corrosion. Reed waste is a natural, abundantly available, and yearly renewable source, acting as the single precursor for Si containing-carbon substrate. The typical product (Si-Fe20/N/C1_6 in this work) possesses a high BET specific surface area, porous structure with high pyridinic-N and pyrrolic-N content. The X-ray absorption near edge structure (XANES), Raman, X-ray photoelectron spectroscopy (XPS) measurements and electrochemical measurements show that Si facilitates incorporation of more N to coordinate with Fe in the porous carbon and induces more graphitic carbon in the catalyst. The sample Si-Fe20/N/C1_6 exhibits better activity and superior stability than the Fe20/N/C counterpart and commercial Pt/C catalyst for the oxygen reduction reaction (ORR) in 0.1 M KOH electrolyte. The results suggest a promising route based on economical and sustainable biomass towards the development and engineering of value-added carbon materials as robust catalysts for oxygen reduction.

1. Introduction

Oxygen reduction reaction (ORR) is a pivotal process in clean renewable energy conversion systems such as fuel cells and metal-air batteries. Currently, the most efficient and widely used ORR catalysts are platinum group metal (PGM) materials, wherein Pt is the most efficient. However, the high cost and scarcity of PGMs seriously restrict their large-scale commercialization. Therefore, the development of low-cost and high-performance non-precious metal catalysts (NPMCs) for ORR is extremely imperative. Among various NPMCs, Fe- and N-doped carbon (Fe/N/C) materials have emerged as the most promising catalysts, in which, the ORR properties are mainly attributed to metal-containing active sites (usually labeled as FeN_x or even FeN_4) [1–3]. Another promising NPMCs is the so-called “metal free” catalysts (MFCs), in which no metal atoms are introduced. For MFCs, heteroatom doping is considered as an effective strategy to enhance the ORR activity by changing the electronic structure of adjacent carbon and/or producing additional active sites, extensive work has been committed

to developing metal-free ORR electrocatalysts, such as doping N-[4–11], S-[12,13], P-[14,15], B-[16,17], F-[18–20], Si-[21,22], and/or their co-doping, tri-doping carbon materials [23–27]. However, fewer research has been investigated on heteroatom doped Fe/N/C catalyst, except some work on S-doped Fe/N/C [28–30] and B-doped Fe/N/C [31] recently, in which the synergistic effects between the heteroatom and Fe/N structure further promote the ORR performance. On the other hand, great efforts have been achieved in high performance NPMC catalysts by using expensive or toxic materials as starting precursors. From a more sustainable perspective, lots of research on the doping carbon materials has moved from expensive, often hazardous inorganic and/or organic chemicals to renewable biomass waste as precursors, mainly for sustainable consideration [32–37].

For the carbon-based electrocatalysts, it is widely accepted that graphitization of the carbon is beneficial in enhancing the conductivity and avoiding the chemical attack, thus improving the stability of the catalysts. It is also interesting to note that Si was proposed to promote the graphitization processes in the catalysts [38,39]. It has been known

* Corresponding authors.

E-mail addresses: gaixia.zhang@emt.inrs.ca (G. Zhang), shuhui@emt.inrs.ca (S. Sun).

¹ These authors contributed equally.

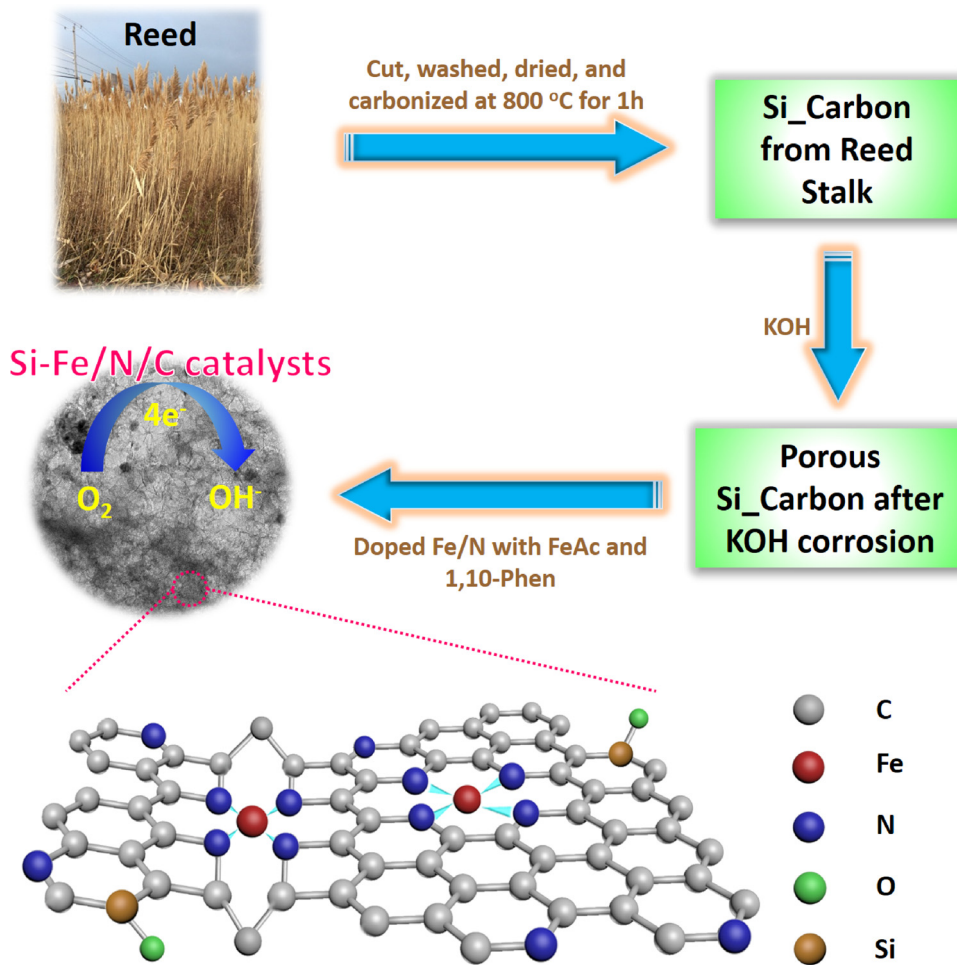


Fig. 1. Schematic procedure for the fabrication of porous Si-Fe/N/C from reed waste.

that Si exists in reed, a sustainable plant that are widely distributed worldwide [40]. In a very favorable nanoscale arrangement, this sustainable Si source has been exploited as anodes for lithium ion batteries [41]. In this work, inspired by the Si-promoting graphitization findings, based on the reed waste, Si contained Fe/N/C (Si-Fe/N/C) catalyst was synthesized by a simple route (Fig. 1). The strategy was to use a cost-effective and easily available natural reed as a single precursor with both Si and C, to fabricate Si-Fe/N/C catalysts. To the best of our knowledge, there is no report on Si-containing Fe/N/C synthesized from natural reed and its use for the ORR yet.

2. Experimental

2.1. Materials

Iron (II) acetate (95 %), 1,10-phenanthroline (99%), hydrochloric acid (HCl, 32% in H₂O) and potassium hydroxide (KOH, 87.1%), were purchased from Fisher Scientific; Reed stalk was obtained from a local farmland in Varennes (Quebec). All chemicals were used as received and solutions were prepared with deionized water (Millipore Milli-Q, 18.2 MΩ cm).

2.2. Preparation of porous Si-contained carbon precursor

The procedure of the preparation of porous carbons from reed was summarized in Fig. 1. Before carbonization, the reed were carefully cut into small pieces, washed with de-ionized (DI)-water, and dried in oven at 80 °C for 2 days. The dried samples were pre-carbonized in

combustion boat at 800 °C for 1 h under Ar flow. Afterwards, the pre-carbonized materials were mixed with KOH at different amount and grind together (weight ratio of materials/KOH is 1:2, 1:6 and 1:10, named as RC1_xKOH, where x is the ratio of KOH/carbon). After that, the mixture was heated in a homemade copper boat under Ar flow at 700 °C for 1 h. Then the porous carbon after KOH corrosion was served as the carbon host for loading Fe and N in the next step. To investigate the effects of Si on the catalyst, some of the carbonized materials before KOH corrosion were leached by HF to remove the Si atoms, followed by mixing with KOH and doping Fe/N in the same way.

2.3. Preparation of Si-Fe/N/C catalysts

In a typical synthesis of Fe/N/C catalyst, taking Si-Fe20/N/C1_6 (simplified as Si-Fe/N/C) as an example, the precursors were prepared by first mixing 100 mg RC1_6KOH, 55 mg 1,10-phenanthroline, 20 mg iron(II) acetate in a solution of ethanol and DI-water under stirring at room temperature. Then the mixture was heated to 60–80 °C for 2–3 h until about 20–25 ml of thick slurry was obtained. The slurry was placed overnight in a drying oven at 95 °C. Afterwards, the dry powder was ground sufficiently and placed in the quartz tube, followed by heating at 1050 °C in Ar for 1 h, and another pyrolysis in ammonia at 950 °C with weight losses around an optimum value of 50% [1,42–45]. In the experiment, different amount of FeAc were used (10, 20, and 30 mg) to find the optimal Fe content of the Si-Fe/N/C catalysts.

Table 1
Electrochemical parameters for Si-Fe20/N/C-1_y.

Samples	Potential values		Current density Kinetic current at 0.9 V
	Onset potential ^a	Half-wave potential	
Si-Fe20/N/C-1_2	0.91 V	0.79 V	0.20 mA cm ⁻²
Si-Fe20/N/C-1_6	1.00 V	0.88 V	4.1 mA cm ⁻²
Si-Fe20/N/C- 1_10	0.99 V	0.85 V	0.92 mA cm ⁻²

^a we define the potential at -0.2 mA cm⁻² as onset potential in this work.

2.4. Physical characterizations

The crystal structure of the as-prepared samples was characterized by X-ray diffraction (XRD, Bruker D8 Advanced Diffractometer, Cu K α radiation). The morphological structures of the catalysts were imaged by using a JEOL 2100F TEM. XPS data was obtained by using a VG ESCALAB 220i-XL equipped with a Twin Anode X-Ray Source, and analysed by Casa XPS software (2.3.15 Version). The C 1s peak (BE = 284.6 eV) was used as the reference line to accurately determine the positions of other spectral lines. The specific surface areas of the catalysts were measured through N₂ sorption isotherms that were collected using Quantachrome Instruments Autosorb-1 at liquid nitrogen temperature (77.3 K), with the Quenched solid density functional theory (QSDFT) available in the AS1WIN software. Raman spectroscopy (Renishaw Imaging Microscope Wire™) was performed using the 785 nm laser radiation with a circular polarization. The laser beam was focused onto the sample to a spot size of 1 μ m. X-ray absorption near edge structure (XANES) measurement was performed at the Canadian Light Source (CLS) (Saskatoon, Canada) on the Variable Line Spacing Plane Grating Monochromator (VLS-PGM) beamline [46]. All the powder samples were smeared on carbon tape as a thin layer and placed in the vacuum chamber of the beamline for the measurement. The XANES spectra were collected in both total electron yield (TEY) and fluorescent yield (FLY) mode [47] (only TEY is presented in this work) with a chamber pressure better than 1×10^{-7} torr at room temperature [48]. The beamline slits sizes were 50 μ m x 50 μ m with an instrumental resolution E/ Δ E > 10,000. The data are normalized by the I₀ current, which is measured by a Nickel mesh placed in front of the sample.

2.5. Electrochemical measurements

All electrochemical measurements were performed in a three-electrode cell using a rotating ring disk electrode (RRDE, PINE Research Instrumentation), a saturated calomel electrode (SCE) and Pt wire were used as the reference and counter electrodes, respectively, as described in our previous study [44,45]. The catalyst suspension in this work was prepared as the following: 10 mg of catalyst was mixed with 95 μ L of 5 wt% Nafion solution and 350 μ L of ethanol in a glass vial (the Nafion-to-catalyst ratio is ~40%), followed by sonication and agitation for 1 h. Then 9 μ L of the catalyst suspension was dropped onto the GC electrode surface (~0.8 mg cm⁻²). For comparison, the 20 wt% Pt/C catalyst (E-ETK) with a loading of 100 μ g cm⁻² was prepared. In order to keep the gas-saturated in the solution, N₂ (or O₂) was bubbled through the electrolyte for 30 min before testing and kept bubbling during the measurements. The linear sweep voltammograms (LSV) were recorded between 0–1.2 V (vs. RHE) with 10 mV s⁻¹ at rotation speed of 1600 rpm, and plotted after subtraction of the background non-Faradic current recorded in N₂-saturated solution. For detecting peroxide formed at the disc electrode, the ring potential was set at 1.3 V. The collection efficiency was N = 0.37. The electron transfer number (n) and peroxide yield (H₂O₂%) were calculated as follows:

$$\text{H}_2\text{O}_2\% = 200 \times (\text{I}_r/\text{N}) / (\text{I}_d + \text{I}_r/\text{N})$$

$$n = 4 \times \text{I}_d / (\text{I}_d + \text{I}_r/\text{N})$$

Where I_d is the disk current and I_r is the ring current.

The stability of the catalysts was tested on fresh electrodes by chronoamperometry at 0.8 V (vs. RHE) for 20,000 s in O₂-saturated 0.1 M KOH at a rotation speed of 1600 rpm (and 1 day without rotation). In addition, the catalysts were assessed by cycling over 10,000 cycles between 0.6 and 1.0 V at 100 mV s⁻¹ under O₂-saturated electrolyte, which is a more common and standard protocol to evaluate the stability [49–51]. The methanol crossover effects were recorded by adding 4 mL methanol into the 100 mL O₂-saturated 0.1 M KOH solution in the chronoamperometric measurement.

3. Results and discussion

To investigate the impact of the ratio of carbon/KOH and Fe content on our catalysts, we first examined the ORR activity of the Si-Fe_xN/C-1_y catalysts (x is the amount of Fe added, y is the ratio of KOH to carbon), with RDE measurements performed in 0.1 M KOH electrolyte. As shown in Fig. S1, by comparing the half-wave potential and Tafel slope in lower over-potential area (Table 1), it can be obtained: (i) Si-Fe20/N/C1_6 shows the best activity as 1) it has the most positive half-wave potential (0.88 V vs. RHE) than Si-Fe20/N/C1_2 (0.79 V) and Si-Fe20/N/C1_10 (0.85 V), though these three samples have very similar Tafel slope, and 2) the kinetic current density at 0.9 V has the order of Si-Fe20/N/C1_6 (4.1 mA cm⁻²) > Si-Fe20/N/C1_10 (0.92 mA cm⁻²) > Si-Fe20/N/C1_2 (0.20 mA cm⁻²). These results indicate that Si-C1_6KOH is the optimized carbon host. This benefit from the KOH activation plays an important role in the development of the micro-pore structure. As shown in Fig. S2 and Table S1, Si-C1_6 has the largest micro-pore surface area, which provides the possibility to host for the FeN_x active sites [52]. (ii) Fe content has certain effects on the catalytic performance in the catalysts, as shown in Fig S1b and 1d, where it is seen that the Si-Fe20/N/C1_6 has more positive half-wave potential and higher kinetic current density at 0.9 V than other catalysts. This demonstrates that optimal activity can be achieved by tuning the Fe content (too low of Fe content results in too few active sites, and too much Fe results in agglomeration).

The morphology of the as-prepared porous Si-C and Si-Fe/N/C samples from waste reed stalks was investigated by TEM and HR-TEM. Activated carbons are normally composed of randomly stacked graphite-like planes with a high level of disorder (Fig. 2b), associated with a high porosity and specific surface area. The Si-C1_6 in this work displayed a spongy and porous structure, suggesting a large specific surface area. From Fig. 2d and e, after doping with Fe and N, the obtained Si-Fe/N/C has a typical 3D network with open-hollow and interconnected pores (as indicated in the red circles in Fig. 2e), which is expected to offer more active sites for ORR [52]. From Fig. 2e, the graphitic carbon could be clearly observed, possibly due to metal-promoted dissolution-recrystallization [53] and Si-promoted graphitization effects [38]. In addition, NH₃ pyrolysis removed part of amorphous carbon, resulting in the open and hollow structure (Fig. 2d–e). The graphitization carbon could enhance the corrosion resistance, thus improving the stability of the catalysts [54]. By investigating the BET specific surface area of activated porous carbon with different ratios of KOH, it can be obtained that the specific surface area of Si-C-1_6 (1873 m² g⁻¹) is higher than both Si-C-1_2 (826.9 m² g⁻¹) and Si-C-1_10 (1537 m² g⁻¹). Fig. 2c and f presents the N₂ adsorption/desorption isotherms and pore-size distribution (PSD) of the Si-C1_6 and its derived Si-Fe20/N/C. Fig. 2c showed a typical type-I isotherm, which has relative large microporous structures and small external surfaces. The absorption takes place at a very low relative pressure as monolayer absorption. Once the micropores are full filled, the absorption on the external surface are very small [55]. While, after doping Fe and N, Fig. 2f (Si-Fe20/N/C1_6) and Fig. S3 (the Fe20/N/C1_6 counterpart) showed an obvious microporous and a small hysteresis loop. This

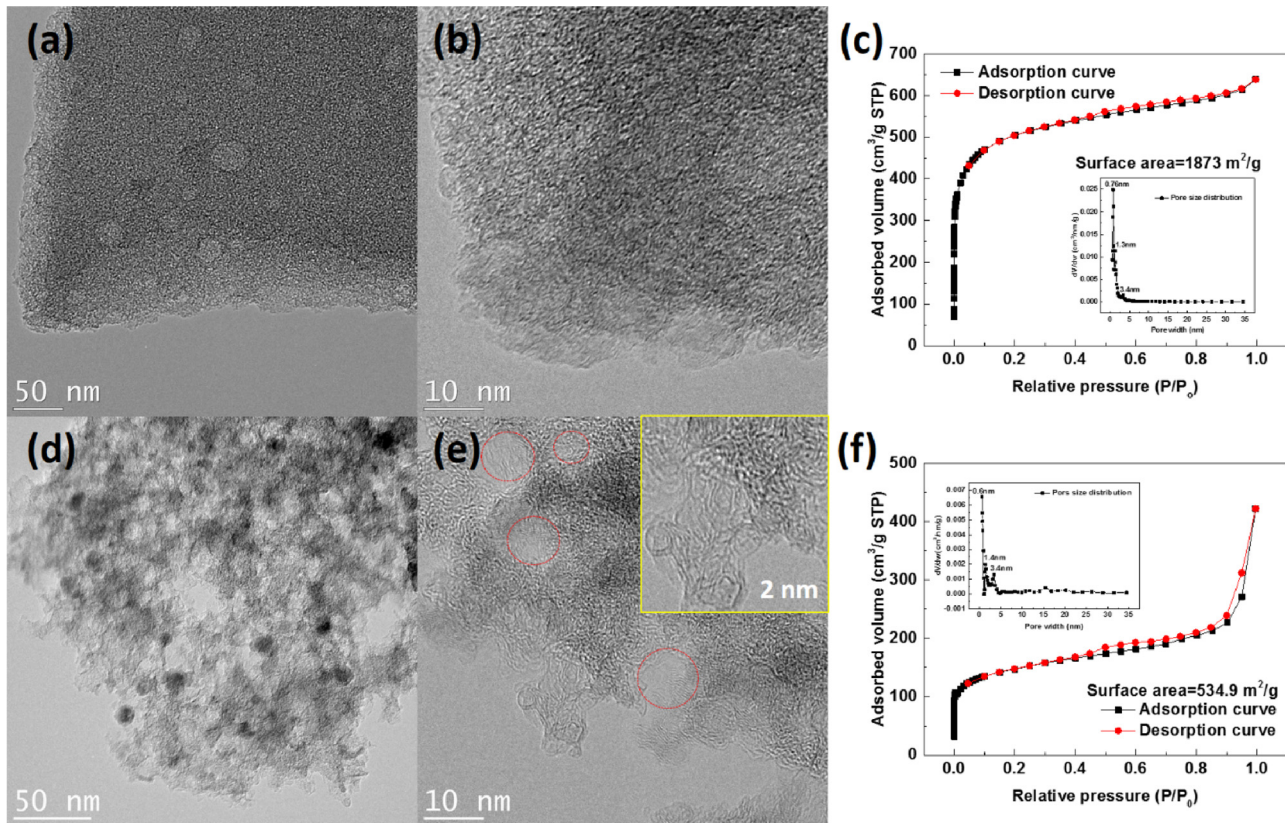


Fig. 2. (a–b) TEM images of porous Si-RC1_6 at different magnifications; (c) N_2 -adsorption/desorption isotherms of Si-RC1_6; (d–e) TEM images of porous Si-Fe/N/C from Si-RC1_6 at different magnifications; (f) N_2 -adsorption/desorption isotherms of porous Si-Fe20/N/C1_6.

indicates the coexistence of micropores and mesopores with solids consisting of agglomerates of particles forming slit shaped pores (plate structure) [56]. Table S2 lists the porous structure characteristics as two ranges: micropores ($< 2.0 \text{ nm}$), and mesopores ($2 \leq d \leq 35 \text{ nm}$). From it, we can see that the Si-Fe/N/C samples possess larger portion of micropores (where is believed the main host for the active sites) than the corresponding Fe/N/C catalyst. It should be noted that Si-Fe20/N/C has relative small area but shows the best activity. This is caused by the Fe content effect (another factor on the ORR performance) as discussed in this work and our previous work [44]. The specific surface area of the counterpart Fe20/N/C1_6 sample is $479.1 \text{ m}^2 \text{ g}^{-1}$ (vs. $534.9 \text{ m}^2 \text{ g}^{-1}$ of Si-Fe20/N/C1_6) with less micropores and more mesopores between $3.3\text{--}5.9 \text{ nm}$ (Fig. S3), which is due to the corrosion of HF treatment of the porous carbon.

XPS, Raman and XANES analysis were carried out to investigate the elemental composition and chemical status. The typical XPS survey spectrum (Fig. S5) indicates the existence of C, O and Si in porous Si-RC1_6 derived from the natural reed stalks, after the HF treatment, the Si element was removed successfully. After doping with Fe and N, it can be found the existence of Fe, N, C, O and Si in porous Si-Fe20NC_RC1_6 from the XPS survey spectrum (Fig. 3a). For comparison, based on the porous carbon without Si, the corresponding Fe/N/C sample was prepared with the same preparation method and the XPS survey spectrum further confirmed the absence of Si (Fig. 3a). The Si 2p peaks at $\sim 102 \text{ eV}$ and $\sim 105 \text{ eV}$ show the presence of the chemical bonds of $-\text{C}-\text{Si}-\text{O}-$ and SiO_2 in the Si-Fe20/N/C1_6 sample (Fig. S6). The high-resolution N 1s XPS spectrum (Fig. 3b) of Si-Fe20/N/C and Fe20/N/C can be deconvoluted into four main peaks: namely pyridinic N, pyrrolic N, graphitic N and N oxides, their contents are also listed in Fig. 3b. From it, it can be found that more pyridinic N and pyrrolic N are existed in Si-Fe20/N/C than Fe20/N/C. As known, the peaks of N coordinated with Fe, either as a porphyrin-like $\text{Fe}^{II}\text{N}_4\text{C}_{12}$ structure or $\text{FeN}_{2+2}/\text{C}$

model [57,58], should be subjected to pyridinic N and pyrrolic N, thus, it can be deduced that the existence of Si may promote more N to coordinate with Fe. The graphitic structure of the Si-Fe20/N/C1_6 and Fe20/N/C1_6 was further studied by Raman analysis (Fig. 3c). As it is well known, G band around 1640 cm^{-1} corresponds to the E_{2g} symmetry of graphitic sp^2 bonded carbon, and the D band peak located around 1340 cm^{-1} is caused by the defects and disorders in the hexagonal graphitic layers. By comparison of the intensity ratios of the I_D/I_G , it can be found that the proportion of graphitic carbon is enhanced in the Si-containing Fe/N/C sample (1.78 vs. 1.34 of the Si-absent Fe/N/C sample), indicating the graphitization effects of Si [38,39].

Figs. 3d and S7 are the Si L_{2,3}-edge XANES spectra for the standard model Si wafer and the Si-containing samples in this work. For all the samples, three well resolved main peaks (a–c) can be observed. The intense peak c is caused by the transition of Si 2p electrons to 3s or 3d-like orbitals [59]. Closer observation revealed an energy shift for the Si-Fe20/N/C sample compared with the Si wafer and its precursor Si-containing porous carbon, indicating that the different local chemistry environment of Si and the participation of Si during the Fe and N doping process. The two peaks a ($\sim 105.5 \text{ eV}$) and b ($\sim 106.1 \text{ eV}$) are the fingerprints of SiO_2 due to the formation of tetrahedron bonds of Si with O, which can be attributed to transitions of 2p electrons to unoccupied 3d orbitals which were split by the 2p spin-orbit splitting [59,60]. It has been reported that the intensity ratio a/b can be used as a reference to differentiate the samples [61]. In the samples of this work, the surface sensitive TEY spectra clearly track Si-O bond in Si wafer due to surface oxidation. Precursor Si-containing porous carbon exhibits similar and sharper features with slight higher resonance than that of Si wafer, illustrating better crystallization upon carbonization. After doping with Fe and N, the a/b ratio is greatly reduced, where peak a is greatly suppressed to a broad shoulder due to the incorporation of Fe and N. From Fig. S8 and Table S3, it can be found that

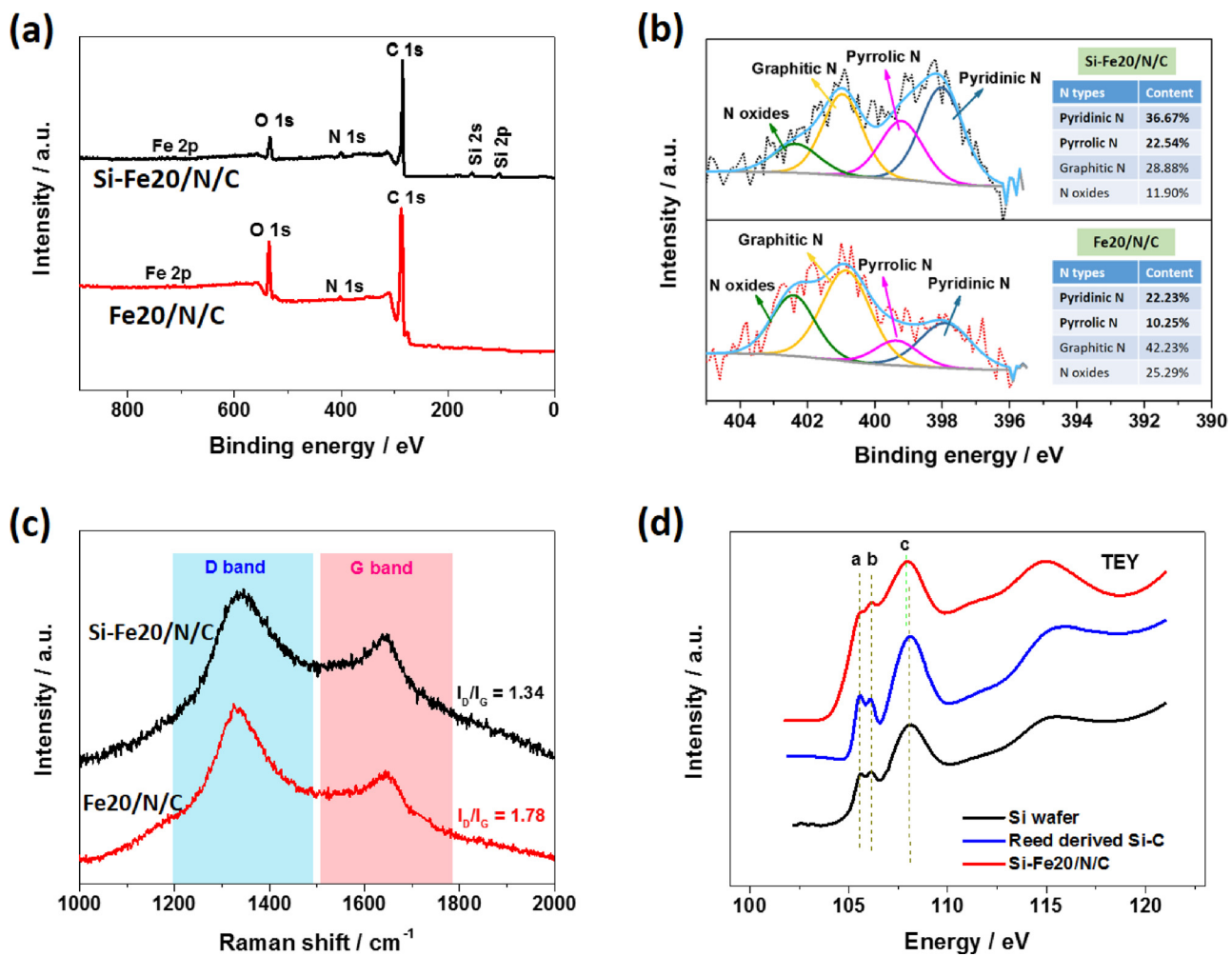


Fig. 3. (a) XPS survey spectra of Si-Fe20/N/C1₆, and Fe20/N/C1₆ (prepared based on the HF treated reed derived porous carbon), (b) core level N 1 s XPS spectrum of Si-Fe20/N/C1₆ and Fe20/N/C, (c) Raman spectra of Si-Fe20/N/C1₆ and Fe20/N/C1₆, (d) Si L_{2,3}-edge XANES spectra of model Si wafer, reed derived porous Si-containing carbon and the prepared Si-Fe20/N/C.

the lower of the a/b ratio, the higher activity of the catalyst performs at 0.9 V is, indicating that the Fe content in the precursor for Si-Fe20/N/C is the optimized amount for suppressing the a peak. Although the mechanism behind the a/b ratio and ORR activity is not clear yet, these distinct features reveal the participation of Si during the doping process, which is directly related with the formation of more graphitic carbon and the specific nitrogen configuration, as demonstrated from Raman and XPS results. Furthermore, Fig. 4a and d show the C1s spectrum of Si-Fe20/N/C and Fe20/N/C, the peak located at 284.6 eV is related to the sp² C=C band of graphitic carbon. Obviously, the component of sp² C=C in the Si-Fe20/N/C (62.2%) is higher than that of Fe20/N/C (38.6%). To further confirm the enhanced graphitic structure character of Si-Fe20/N/C, more HRTEM images were taken randomly for both samples, as shown in Fig. 4b and c for Si-Fe20/N/C, turbostratic structure of graphitic is clearly present; comparatively, for Fe20/N/C, only weak layered graphitization structure can be observed (Fig. 4e and f). These results confirmed the graphitization effects of Si in a more direct way, consisting with the previous analysis.

To gain insight into the ORR activity, we examined the electrocatalytic properties of Si-Fe20/N/C1₆ by employing a rotating ring-disk electrode (RRDE) technique in a N₂- and O₂-saturated 0.1 M aqueous KOH electrolyte solution at a scan rate of 10 mV s⁻¹ at a rotation speed of 1600 rpm. The amount of H₂O₂ generated at the disk electrode and the electron transfer number (n) could be accurately calculated from RRDE. For comparison, the Fe20/N/C1₆ prepared

based on the HF treated porous carbon and the commercial Pt/C were also measured with the same condition as Si-Fe20/N/C1₆. The onset potential for the ORR is an important criterion to evaluate the activity of an electrocatalyst. Fig. 4a is the LSV curves of these three samples, it can be seen that both Si-Fe20/N/C1₆ and Fe20/N/C1₆ have more positive onset potential (0.99 V) than Pt/C (0.91 V). This demonstrates the excellent catalytic activity for ORR of the reed-derived NPMCs. Interestingly, though the onset potential suggests very similar kinetics between Fe20/N/C and Si-Fe20/N/C1₆, the existence of Si in Si-Fe20/N/C1₆ has positive effects to the mixed kinetic-diffusion controlled region. Fig. S9 shows the Tafel plots of catalysts. A low value of Tafel slope is highly advantageous, and indicates a more efficient electrochemical process. To see more differences of the two samples with and without Si doping, we divided 2 zones in Fig. S9. The Tafel slope at higher potentials (zone 1) usually suggests that ORR rate is determined by oxygen intermediates absorption (corresponding to the on-set potential). The two catalysts have very similar values in zone 1, but with different Tafel slopes (82 mV dec⁻¹ for Si-Fe20/N/C1₆ vs 93 mV dec⁻¹ for Fe20/N/C1₆) showing the better kinetics of the former catalyst. In zone 2, at lower potentials, we can regard it as the mixed region of the kinetics and diffusion. Obviously, Si-Fe20/N/C1₆ has a much smaller slope than Fe20/N/C1₆ (95 mV dec⁻¹ vs 120 mV dec⁻¹), showing its high efficient electrochemical process. Notably, the electron transferred number (n) of Si-Fe20/N/C1₆ displays very close value with the commercial Pt/C over a potential range of 0.2–0.8 V

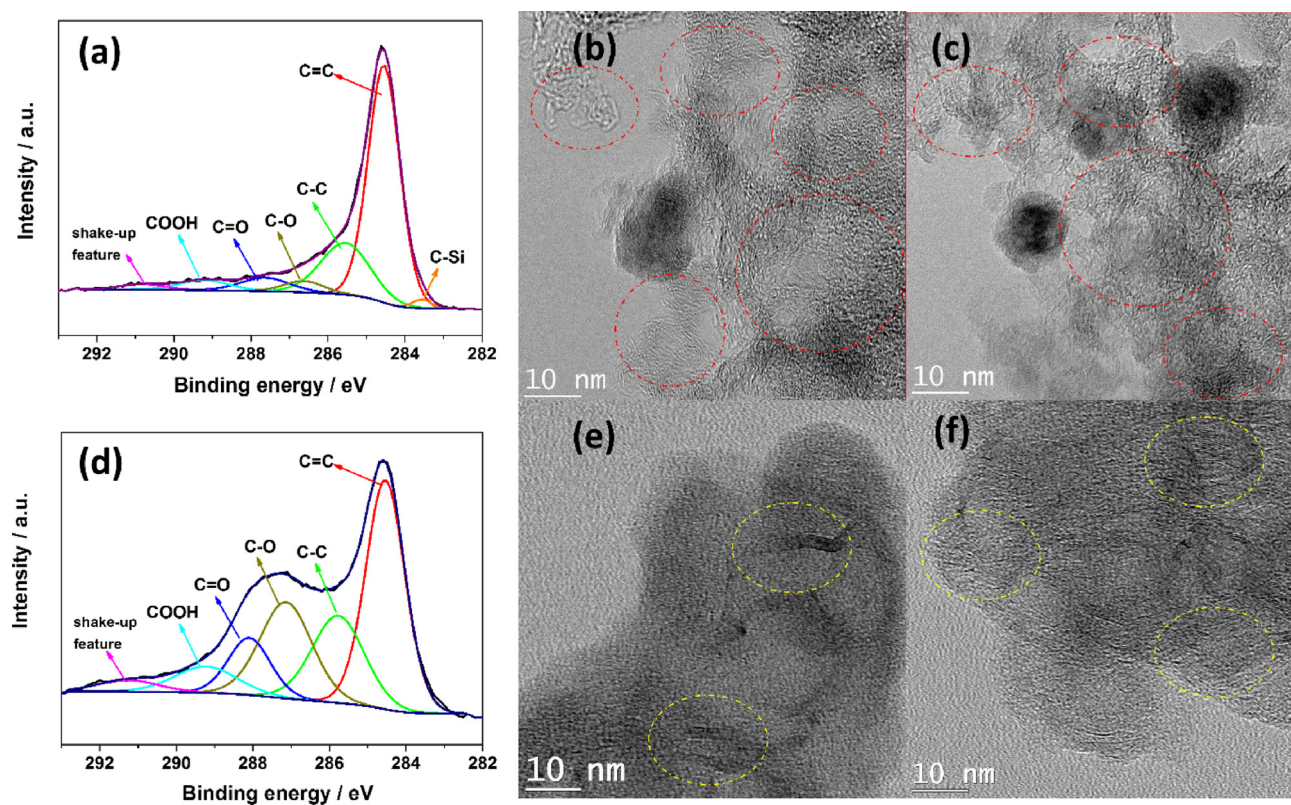


Fig. 4. (a, d) Core level C 1 s XPS spectrum of Si-Fe20/N/C and Fe20/N/C, (b, c) HRTEM images of Si-Fe20/N/C, (e, f) HRTEM images of Fe20/N/C.

(Fig. 4b), implying a high selectivity toward one-step oxygen reduction to water. By calculating, the measured H_2O_2 yield of Si-Fe20/N/C1_6 is below 6% in the measured potential range, even lower than the corresponding Fe20/N/C1_6 sample (Fig. 4b), demonstrating its higher ORR catalytic efficiency.

The durability is an important factor for evaluating the performance of ORR catalysts. Fig. 4c shows that the current density of the Si-Fe20/N/C1_6 catalyst remains 94.8% after 20,000 s at a rotation speed of 1600 rpm under 0.8 V (vs. RHE), which is apparently higher than that of the Fe20/N/C1_6 catalyst (83.3%) and commercial Pt/C catalyst (65.5%) in the same condition. A long-term chronoamperometric stability evaluation (at 0.8 V vs. RHE) showed no significant loss in ORR activity after ~ 24 h of continuous measurement (Fig. S10), indicating that Si-Fe20/N/C1_6 is able to sustain a stable ORR performance over a long period of time. Moreover, we further evaluated the stability by assessing the LSV curves after cycling the electrode potential between 0.6–1.0 V under O_2 -saturated electrolyte. The results are shown in Fig. S11 and Fig. 5e, only ~ 12 mV of change can be observed for Si-Fe20/N/C at 3 mA cm^{-2} , lower than that of Fe20/N/C (~ 19 mV) and Pt/C (~ 40 mV). The higher stability of Si-Fe20/N/C1_6 might be attributed to the higher graphitization of the carbon structure (probably promoted by Si) [38,39] in it. Methanol crossover effect should be considered in fuel cells that use methanol as the fuel, because the methanol crossover could severely deteriorate the ORR performance on the cathode. So the methanol tolerant ability of the Si-Fe20/N/C1_6 catalyst and the commercial Pt/C catalyst in 0.1 M KOH electrolyte are compared. As illustrated in Fig. 4d, the Pt/C catalyst suffers from remarkable loss in current density upon the introduction of methanol into the electrolyte, indicating methanol oxidation on the electrode. On the contrast, the Si-Fe20/N/C1_6 catalyst displays very little change on current density after the introduction of methanol, demonstrating much better resistance to methanol crossover than the Pt/C catalyst.

4. Conclusions

In summary, we have developed an efficient Si-contained Fe/N/C ORR catalyst by using the waste reed stalk as the Si and C source. XANES, Raman and XPS measurements indicate that due to the participating of Si in the Fe/N doping process, the Si-Fe/N/C catalyst possesses enhanced graphitic carbon structure with more nitrogen moieties coordinating with Fe. These features make Si-Fe/N/C catalyst showing good ORR activity, and importantly, Si-Fe/N/C exhibits better stability (with 94.8% retention of the current after 20,000 s under a high voltage of 0.8 V) than the Fe/N/C counterpart (83.3%) and Pt/C (65.5%); and only ~ 12 mV of change at 3 mA cm^{-2} for Si-Fe/N/C after 10,000 potential cycles under O_2 -saturated electrolyte (vs. ~ 19 mV for Fe/N/C and ~ 40 mV for Pt/C), as well as higher tolerance toward methanol compared with Pt/C. Moreover, ORR on the Si-Fe/N/C follows the efficient 4e- pathway. Taking together, our developed Si-Fe/N/C catalyst as a substitute for commercial Pt/C could provide possibility in alkaline fuel cells and other applications with good ORR performance and high stability. We believe that this work will give more insights to design highly stable catalysts for the clean energy related devices and have significant economic and environment effects by making full use of biomass wastes.

Notes

The authors declare no competing financial interest.

Author contributions

The manuscript was written through contributions of all authors. All authors have given approval to the final version of the manuscript.

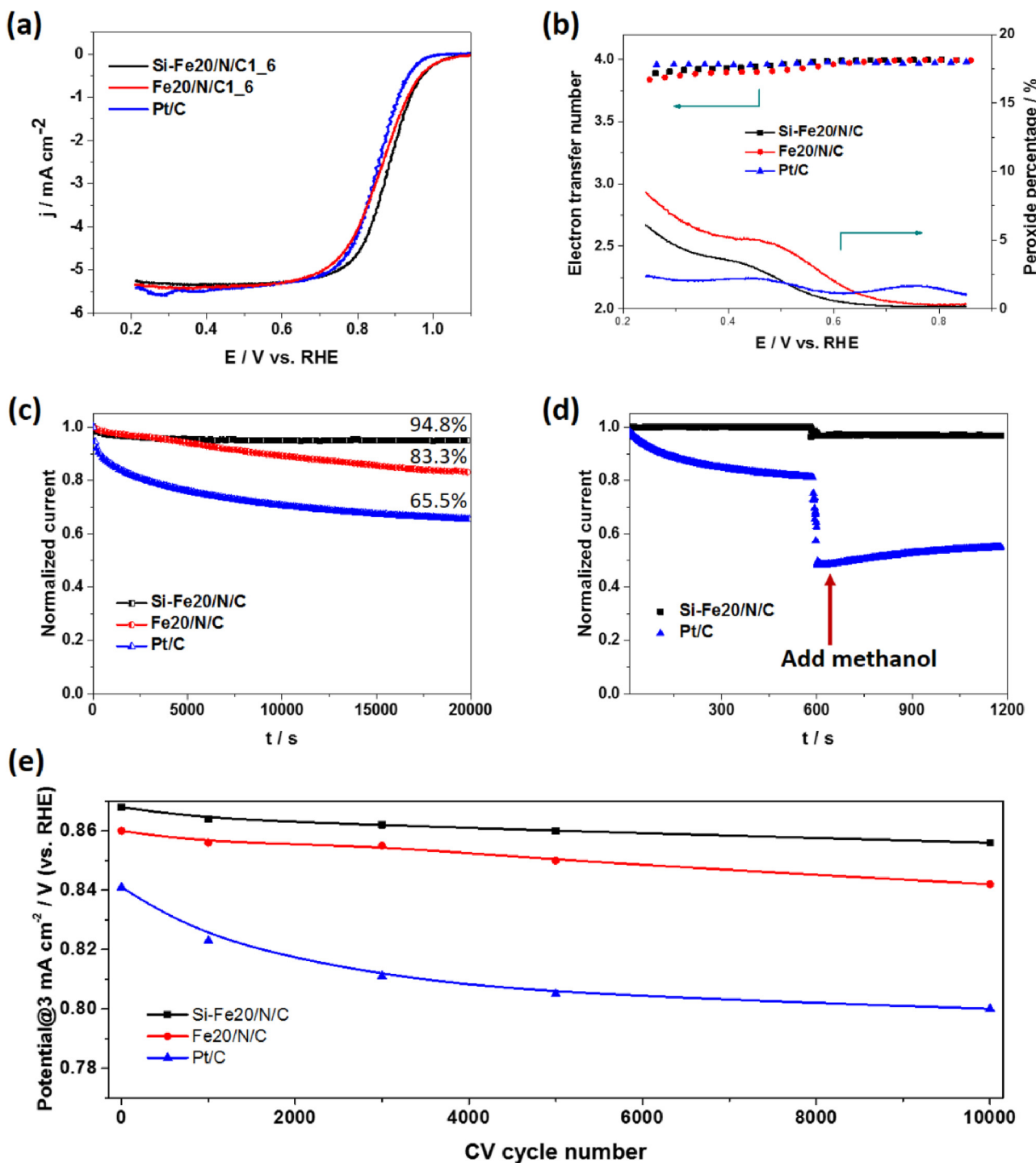


Fig. 5. (a) LSV curves, (b) electron transfer number (n), and H_2O_2 selectivity of Si-Fe20/N/C1_6, Fe20/N/C1_6 and commercial Pt/C in O_2 -saturated 0.1 M KOH at a scan rate of 10 mV s^{-1} , rotation rate = 1600 rpm. (c) Chronoamperometric responses (at 0.8 V vs. RHE) of Si-Fe20/N/C1_6, Fe20/N/C1_6 and commercial Pt/C catalysts in O_2 -saturated 0.1 M KOH with rotation speed of 1600 rpm, (d) chronoamperometric responses of Si-Fe20/N/C1_6 and Pt/C catalysts show the effect of adding 4 mL methanol into the 100 mL O_2 -saturated 0.1 m KOH solution. (e) Potential at 3 mA cm^{-2} of Si-Fe20/N/C1_6, Fe20/N/C1_6 and commercial Pt/C as a function of the number of potential cycles in O_2 -saturated electrolyte.

Acknowledgements

This work is supported financially by the Natural Sciences and Engineering Research Council of Canada (NSERC), Ballard Power Systems Inc., the Fonds de Recherche du Québec-Nature et Technologies (FRQNT), Canada Foundation for Innovation (CFI), Centre Québécois sur les Matériaux Fonctionnels (CQMF), Institut National de la Recherche Scientifique (INRS) and China Scholarship

Council (CSC). Synchrotron research described in this paper was performed at the Canadian Light Source, which is supported by the Canada Foundation for Innovation, the Natural Sciences and Engineering Research Council of Canada (NSERC), the University of Saskatchewan, the Government of Saskatchewan, Western Economic Diversification Canada, the National Research Council Canada, and the Canadian Institutes of Health Research.

Appendix A. Supplementary data

Supplementary material related to this article can be found, in the online version, at doi:<https://doi.org/10.1016/j.apcatb.2018.05.046>.

References

- [1] M. Lefèvre, E. Proietti, F. Jaouen, J.-P. Dodelet, Iron-based catalysts with improved oxygen reduction activity in polymer electrolyte fuel cells, *Science* 324 (2009) 71–74.
- [2] H. Tang, Y. Zeng, Y. Zeng, R. Wang, S. Cai, C. Liao, H. Cai, X. Lu, P. Tsiakaras, Iron-embedded nitrogen doped carbon frameworks as robust catalyst for oxygen reduction reaction in microbial fuel cells, *Appl. Catal. B: Environ.* 202 (2017) 550–556.
- [3] M. Shao, Q. Chang, J.-P. Dodelet, R. Chenitz, Recent advances in electrocatalysts for oxygen reduction reaction, *Chem. Rev.* 116 (2016) 3594–3657.
- [4] K. Gong, F. Du, Z. Xia, M. Durstock, L. Dai, Nitrogen-doped carbon nanotube arrays with high electrocatalytic activity for oxygen reduction, *Science* 323 (2009) 760–764.
- [5] L. Lai, J.R. Potts, D. Zhan, L. Wang, C.K. Poh, C. Tang, H. Gong, Z. Shen, J. Lin, R.S. Ruoff, Exploration of the active center structure of nitrogen-doped graphene-based catalysts for oxygen reduction reaction, *Energy Environ. Sci.* 5 (2012) 7936–7942.
- [6] W. Wei, H. Liang, K. Parvez, X. Zhuang, X. Feng, K. Müllen, Nitrogen-doped carbon nanosheets with size-defined mesopores as highly efficient metal-free catalyst for the oxygen reduction reaction, *Angew. Chem.* 126 (2014) 1596–1600.
- [7] S. Chen, J. Bi, Y. Zhao, L. Yang, C. Zhang, Y. Ma, Q. Wu, X. Wang, Z. Hu, Nitrogen-doped carbon nanocages as efficient metal-free electrocatalysts for oxygen reduction reaction, *Adv. Mater.* 24 (2012) 5593–5597.
- [8] P. Zhang, F. Sun, Z. Xiang, Z. Shen, J. Yun, D. Cao, ZIF-derived *in situ* nitrogen-doped porous carbons as efficient metal-free electrocatalysts for oxygen reduction reaction, *Energy Environ. Sci.* 7 (2014) 442–450.
- [9] D. Guo, R. Shibuya, C. Akiba, S. Saji, T. Kondo, J. Nakamura, Active sites of nitrogen-doped carbon materials for oxygen reduction reaction clarified using model catalysts, *Science* 351 (2016) 361–365.
- [10] K. Wan, G.-F. Long, M.-Y. Liu, L. Du, Z.-X. Liang, P. Tsiakaras, Nitrogen-doped ordered mesoporous carbon synthesis and active sites for electrocatalysis of oxygen reduction reaction, *Appl. Catal. B* 165 (2015) 566–571.
- [11] Q. Wei, X. Tong, G. Zhang, J. Qiao, Q. Gong, S. Sun, Nitrogen-doped carbon nanotube and graphene materials for oxygen reduction reactions, *Catalysts* 5 (2015) 1574–1602.
- [12] Z. Ma, S. Dou, A. Shen, L. Tao, L. Dai, S. Wang, Sulfur-doped graphene derived from cycled lithium–sulfur batteries as a metal-free electrocatalyst for the oxygen reduction reaction, *Angew. Chem.* 54 (2015) 1888–1892.
- [13] L. Zhang, J. Niu, M. Li, Z. Xia, Catalytic mechanisms of sulfur-doped graphene as efficient oxygen reduction reaction catalysts for fuel cells, *J. Phys. Chem. C* 118 (2014) 3545–3553.
- [14] C. Zhang, N. Mahmood, H. Yin, F. Liu, Y. Hou, Synthesis of phosphorus-doped graphene and its multifunctional applications for oxygen reduction reaction and lithium ion batteries, *Adv. Mater.* 25 (2013) 4932–4937.
- [15] D.-S. Yang, D. Bhattacharjya, S. Inamdar, J. Park, J.-S. Yu, Phosphorus-doped ordered mesoporous carbons with different lengths as efficient metal-free electrocatalysts for oxygen reduction reaction in alkaline media, *J. Am. Chem. Soc.* 134 (2012) 16127–16130.
- [16] Z.-H. Sheng, H.-L. Gao, W.-J. Bao, F.-B. Wang, X.-H. Xia, Synthesis of boron doped graphene for oxygen reduction reaction in fuel cells, *J. Mater. Chem.* 22 (2012) 390–395.
- [17] X. Bo, L. Guo, Ordered mesoporous boron-doped carbons as metal-free electrocatalysts for the oxygen reduction reaction in alkaline solution, *Phys. Chem. Chem. Phys.* 15 (2013) 2459–2465.
- [18] X. Sun, Y. Zhang, P. Song, J. Pan, L. Zhuang, W. Xu, W. Xing, Fluorine-doped carbon blacks: highly efficient metal-free electrocatalysts for oxygen reduction reaction, *ACS Catal.* 3 (2013) 1726–1729.
- [19] G. Panomsuwan, N. Saito, T. Ishizaki, Simple one-step synthesis of fluorine-doped carbon nanoparticles as potential alternative metal-free electrocatalysts for oxygen reduction reaction, *J. Mater. Chem. A* 3 (2015) 9972–9981.
- [20] X. Sun, P. Song, T. Chen, J. Liu, W. Xu, Fluorine-doped BP 2000: highly efficient metal-free electrocatalysts for acidic oxygen reduction reaction with superlow H_2O_2 yield, *Chem. Commun.* 49 (2013) 10296–10298.
- [21] Z. Liu, X. Fu, M. Li, F. Wang, Q. Wang, G. Kang, F. Peng, Novel silicon-doped, silicon and nitrogen-codoped carbon nanomaterials with high activity for the oxygen reduction reaction in alkaline medium, *J. Mater. Chem. A* 3 (2015) 3289–3293.
- [22] X. Fu, Q.-D. Wang, Z. Liu, F. Peng, Si-doped carbon nanotubes as efficient metal-free electrocatalysts for O_2 reduction in alkaline medium, *Mater. Lett.* 158 (2015) 32–35.
- [23] Y. Zhao, L. Yang, S. Chen, X. Wang, Y. Ma, Q. Wu, Y. Jiang, W. Qian, Z. Hu, Can boron and nitrogen co-doping improve oxygen reduction reaction activity of carbon nanotubes? *J. Am. Chem. Soc.* 135 (2013) 1201–1204.
- [24] W. Ai, Z. Luo, J. Jiang, J. Zhu, Z. Du, Z. Fan, L. Xie, H. Zhang, W. Huang, T. Yu, Nitrogen and sulfur codoped graphene: multifunctional electrode materials for high-performance Li-ion batteries and oxygen reduction reaction, *Adv. Mater.* 26 (2014) 6186–6192.
- [25] S. Wang, L. Zhang, Z. Xia, A. Roy, D.W. Chang, J.B. Baek, L. Dai, BCN graphene as efficient metal-free electrocatalyst for the oxygen reduction reaction, *Angew. Chem. Int. Ed.* 51 (2012) 4209–4212.
- [26] J. Zhang, Z. Zhao, Z. Xia, L. Dai, A metal-free bifunctional electrocatalyst for oxygen reduction and oxygen evolution reactions, *Nat. Nanotech.* 10 (2015) 444–452.
- [27] Y. Su, Z. Yao, F. Zhang, H. Wang, Z. Mics, E. Cánovas, M. Bonn, X. Zhuang, X. Feng, Sulfur-enriched conjugated polymer nanosheet derived sulfur and nitrogen co-doped porous carbon nanosheets as electrocatalysts for oxygen reduction reaction and zinc–air battery, *Adv. Funct. Mater.* 26 (2016) 5893–5902.
- [28] Y.C. Wang, Y.J. Lai, L. Song, Z.Y. Zhou, J.G. Liu, Q. Wang, X.D. Yang, C. Chen, W. Shi, Y.P. Zheng, S-doping of an Fe/N/C ORR catalyst for polymer electrolyte membrane fuel cells with high power density, *Angew. Chem.* 127 (2015) 10045–10048.
- [29] K. Hu, L. Tao, D. Liu, J. Huo, S. Wang, Sulfur-doped Fe/N/C nanosheets as highly efficient electrocatalysts for oxygen reduction reaction, *ACS Appl. Mater. Interfaces* 8 (2016) 19379–19385.
- [30] P. Chen, T. Zhou, L. Xing, K. Xu, Y. Tong, H. Xie, L. Zhang, W. Yan, W. Chu, C. Wu, Atomically dispersed iron–nitrogen species as electrocatalysts for bifunctional oxygen evolution and reduction reactions, *Angew. Chem.* 56 (2017) 610–614.
- [31] K. Yuan, S. Sfaelou, M. Qiu, D.F. Lützenkirchen-Hecht, X. Zhuang, Y. Chen, C. Yuan, X. Feng, U. Scherf, The synergistic contribution of boron and Fe–N_x species in porous carbons towards efficient electrocatalysts for oxygen reduction reaction, *ACS Energy Lett.* 3 (2018) 252–260.
- [32] S. Gao, K. Geng, H. Liu, X. Wei, M. Zhang, P. Wang, J. Wang, Transforming organic-rich amaranthus waste into nitrogen-doped carbon with superior performance of the oxygen reduction reaction, *Energy Environ. Sci.* 8 (2015) 221–229.
- [33] M.Y. Song, H.Y. Park, D.S. Yang, D. Bhattacharjya, J.S. Yu, Seaweed-derived heteroatom-doped highly porous carbon as an electrocatalyst for the oxygen reduction reaction, *ChemSusChem* 7 (2014) 1755–1763.
- [34] J. Wei, Y. Liang, Y. Hu, B. Kong, G.P. Simon, J. Zhang, S.P. Jiang, H. Wang, A versatile iron–tannin–framework ink coating strategy to fabricate biomass-derived iron carbide/Fe–N–carbon catalysts for efficient oxygen reduction, *Angew. Chem.* 128 (2016) 1377–1381.
- [35] P. Chen, L.-K. Wang, G. Wang, M.-R. Gao, J. Ge, W.-J. Yuan, Y.-H. Shen, A.-J. Xie, S.-H. Yu, Nitrogen-doped nanoporous carbon nanosheets derived from plant biomass: an efficient catalyst for oxygen reduction reaction, *Energy Environ. Sci.* 7 (2014) 4095–4103.
- [36] S. Gao, Y. Chen, H. Fan, X. Wei, C. Hu, H. Luo, L. Qu, Large scale production of biomass-derived N-doped porous carbon spheres for oxygen reduction and supercapacitors, *J. Mater. Chem. A* 2 (2014) 3317–3324.
- [37] C. Zhu, J. Zhai, S. Dong, Bifunctional fluorescent carbon nanodots: green synthesis via soy milk and application as metal-free electrocatalysts for oxygen reduction, *Chem. Commun.* 48 (2012) 9367–9369.
- [38] Q. Lin, Z. Feng, Z. Liu, Q. Guo, Z. Hu, L. He, H. Ye, Atomic scale investigations of catalyst and catalytic graphitization in a silicon and titanium doped graphite, *Carbon* 88 (2015) 252–261.
- [39] A.B. García, I. Cameán, I. Suelves, J.L. Pinilla, M.J. Lázaro, J.M. Palacios, R. Moliner, The graphitization of carbon nanofibers produced by the catalytic decomposition of natural gas, *Carbon* 47 (2009) 2563–2570.
- [40] E. Epstein, Silicon: its manifold roles in plants, *Ann. Appl. Biol.* 155 (2009) 155–160.
- [41] J. Liu, P. Kopold, P.A. van Aken, J. Maier, Y. Yu, Energy storage materials from nature through nanotechnology: a sustainable route from reed plants to a silicon anode for lithium-ion batteries, *Angew. Chem.* 127 (2015) 9768–9772.
- [42] E. Proietti, F. Jaouen, M. Lefèvre, N. Larouche, J. Tian, J. Herranz, J.-P. Dodelet, Iron-based cathode catalyst with enhanced power density in polymer electrolyte membrane fuel cells, *Nat. Commun.* 2 (2011) 416.
- [43] G. Zhang, R. Chenitz, M. Lefèvre, S. Sun, J.-P. Dodelet, Is iron involved in the lack of stability of Fe/N/C electrocatalysts used to reduce oxygen at the cathode of PEM fuel cells? *Nano Energy* 29 (2016) 111–125.
- [44] Q. Wei, G. Zhang, X. Yang, R. Chenitz, D. Banham, L. Yang, S. Ye, S. Knights, S. Sun, 3D porous Fe/N/C spherical nanostructures as high-performance electrocatalysts for oxygen reduction in both alkaline and acidic media, *ACS Appl. Mater. Interfaces* 9 (2017) 36944–36954.
- [45] Q. Wei, G. Zhang, X. Yang, Y. Fu, G. Yang, N. Chen, W. Chen, S. Sun, Litchi-like porous Fe/N/C spheres with atomically dispersed FeN_x promoted by sulfur as highly efficient oxygen electrocatalysts for Zn–air batteries, *J. Mater. Chem. A* 6 (2018) 4605–4610.
- [46] Y.F. Hu, L. Zuin, G. Wright, R. Igarashi, M. McKibben, T. Wilson, S.Y. Chen, T. Johnson, D. Maxwell, B.W. Yates, Commissioning and performance of the variable line spacing plane grating monochromator beamline at the Canadian light source, *Rev. Sci. Instrum.* 78 (2007) 083109.
- [47] M. Kasrai, Z. Yin, G.M. Bancroft, K.H. Tan, X-ray fluorescence measurements of X-ray absorption near edge structure at the Si, P, and S L edges, *J. Vac. Sci. Technol. A* 11 (1993) 2694–2699.
- [48] D. Wang, L. Zuin, Li K-edge X-ray absorption near edge structure spectra for a library of lithium compounds applied in lithium batteries, *J. Power Sources* 337 (2017) 100–109.
- [49] L. Osmieri, E.-C. Ricardo, A. Marco, O. Pilar, H.A.M.V. Alessandro, S. Stefania, Effects of using two transition metals in the synthesis of non-noble electrocatalysts for oxygen reduction reaction in direct methanol fuel cell, *Electrochim. Acta* 266 (2018) 220–232.
- [50] A. Ohma, S. Kazuhiko, I. Akihiro, Y. Toshihiko, D. Akimasa, Membrane and catalyst performance targets for automotive fuel cells by FCCJ membrane, catalyst, MEA WG, *ECS Trans.* 41 (1) (2011) 775–784.
- [51] L. Osmieri, Z. Claudio, L. Wang, H.A.M.V. Alessandro, L. Alessandro, S. Stefania, Polypyrrole-derived Fe-Co-N/C catalyst for oxygen reduction reaction: performance in alkaline hydrogen and ethanol fuel cells, *ChemElectroChem* 5 (2018) 1–13.

- [52] F. Jaouen, M. Lefèvre, J.-P. Dodelet, M. Cai, Heat-treated Fe/N/C catalysts for O₂ electroreduction: are active sites hosted in micropores? *J. Phys. Chem. B* 110 (2006) 5553–5558.
- [53] K. Elumeeva, J. Ren, M. Antonietti, T.P. Fellinger, High surface iron/co-balt-containing nitrogen-doped carbon aerogels as non-precious advanced electrocatalysts for oxygen reduction, *ChemElectroChem* 2 (2015) 584–591.
- [54] G. Wu, K.L. More, C.M. Johnston, P. Zelenay, High-performance electrocatalysts for oxygen reduction derived from polyaniline, iron, and cobalt, *Science* 332 (2011) 443–447.
- [55] K.S. Sing, Reporting physisorption data for gas/solid systems with special reference to the determination of surface area and porosity (Recommendations 1984), *Pure Appl. Chem.* 57 (1985) 603–619.
- [56] G. Leofanti, M. Padovan, G. Tozzola, B. Venturelli, Surface area and pore texture of catalysts, *Catal. Today* 41 (1998) 207–219.
- [57] V. Glibin, J.-P. Dodelet, Thermodynamic stability in acid media of FeN₄-based catalytic sites used for the reaction of oxygen reduction in PEM fuel cells, *J. Electrochem. Soc.* 164 (2017) F948–F957.
- [58] R. Chenitz, I.K. Ulrike, M. Lefèvre, V. Glibin, G. Zhang, S. Sun, J.-P. Dodelet, A specific demetalation of Fe-N₄ catalytic sites in the micropores of NC-Ar + NH₃ is at the origin of the initial activity loss of the highly active Fe/N/C catalyst used for the reduction of oxygen in PEM fuel cells, *Energy Environ. Sci.* 11 (2018) 365–382.
- [59] D. Li, G.M. Bancroft, M. Kasrai, M.E. Fleet, X.H. Feng, K.H. Tan, B.X. Yang, High-resolution Si K- and L_{2,3}-edge XANES of α -quartz and stishovite, *Solid State Commun.* 87 (1993) 613–617.
- [60] D. Li, G.M. Bancroft, M. Kasrai, M.E. Fleet, X.H. Feng, K.H. Tan, High-resolution Si and P K- and L-edge XANES spectra of crystalline SiP₂O₇ and amorphous SiO₂-P₂O₅, *Am. Mineral.* 79 (1994) 785–788.
- [61] H. Demirkiran, Y. Hu, L. Zuin, N. Appathurai, P.B. Aswath, XANES analysis of calcium and sodium phosphates and silicates and hydroxyapatite–bioglass®4555 co-sintered bioceramics, *Mater. Sci. Eng. C* 31 (2011) 134–143.